The *Hinode Spectro-Polarimeter*

**B.W. Lites · D.L. Akin · G. Card · T. Cruz · D.W. Duncan · C.G. Edwards ·
D.F. Elmore · C. Hoffmann · Y. Katsukawa · N. Katz · M. Kubo · K. Ichimoto ·
T. Shimizu · R.A. Shine · K.V. Streander · A. Suematsu · T.D. Tarbell · A.M. Title ·
S. Tsuneta**

Abstract The joint Japan/US/UK *Hinode* mission includes the first large-aperture visible-light solar telescope flown in space. One component of the *Focal Plane Package* of that telescope is a precision spectro-polarimeter designed to measure full Stokes spectra with the intent of using those spectra to infer the magnetic-field vector at high precision in the solar photosphere. This article describes the characteristics of the flight hardware of the *Hinode Spectro-Polarimeter*, and summarizes its in-flight performance.

B.W. Lites (✉) · G. Card · D.F. Elmore · K.V. Streander
High Altitude Observatory, National Center for Atmospheric Research, Boulder, CO, USA
e-mail: lites@ucar.edu

Present address:
D.F. Elmore
National Solar Observatory/Sacramento Peak, Sunspot, NM, USA

Present address:
K.V. Streander
National Solar Observatory, Tucson, AZ, USA

D.L. Akin · T. Cruz · D.W. Duncan · C.G. Edwards · C. Hoffmann · N. Katz · R.A. Shine · T.D. Tarbell ·
A.M. Title
Lockheed Martin Solar and Astrophysics Laboratory, Palo Alto, CA, USA

Y. Katsukawa · M. Kubo · A. Suematsu · S. Tsuneta
National Astronomical Observatory of Japan, Tokyo, Japan

K. Ichimoto
Kyoto University, Kyoto, Japan

T. Shimizu
Institute of Space and Astronautical Science, Japan Aerospace Exploration Agency, Kanagawa, Japan

1. Overview of the Spectro-Polarimeter

The *Focal Plane Package* (FPP) of the *Solar Optical Telescope* (SOT) instrument (Tsuneta *et al.*, 2008) on the *Hinode* mission (Kosugi *et al.*, 2007) includes the first precision *Spectro-Polarimeter* (SP) for high-resolution solar observations from space. Data from the many ground-based spectro-polarimetric instruments developed within the last 20 years have demonstrated the power of this observational technique to permit not only the measurement of the magnetic-field vector to much higher precision than traditional vector magnetographs, but also the variations of the magnetic field and other properties of the plasma along the line-of-sight (LOS) and even inferences of unresolved atmospheric structure (see, for example, Bellot Rubio, 2006). Such inferences follow from the high information content of the spectrally resolved line profiles recorded in their full state of polarization (*i.e.* recorded in all four Stokes parameters). The limitation of the SP to record only a one-dimensional slice of the solar surface at a time is offset to some extent by the simultaneous polarimetric measurements of the accompanying *Narrowband Filter Instrument* (NFI). The NFI is also capable of full Stokes polarimetry: polarimetric calibration for the NFI is given by Ichimoto *et al.* (2008), and polarimetric calibration of the FPP *Broad-band Filter Instrument* (BFI) has also been accomplished (Snik *et al.*, 2010). These instruments acting in concert are able to provide a more complete picture of the magnetic and dynamic state within the solar atmosphere than has heretofore been possible from the ground.

The *Hinode*/SP has significant heritage from the *Advanced Stokes Polarimeter* (ASP: Elmore *et al.*, 1992). Unlike ASP, the SP operates only in a fixed band of wavelengths centered on the Zeeman-sensitive Fe I lines at 6302 Å. These lines were chosen for the following reasons:

  i) This closely spaced pair of lines arising from the same multiplet (816) have similar formation properties, yet they differ in sensitivity to the Zeeman effect. When analyzed together, they permit a much more accurate determination of field strengths, magnetic filling factors, and field orientations to the LOS than is possible from a single line.
 ii) Being higher excitation lines, they have smaller sensitivity to temperature than other lines such as those near 5250 Å, hence they are more amenable to simple analyses such as are permitted by a Milne–Eddington model atmosphere.
iii) The lines differ in oscillator strength by a factor of 2.6, and hence the two lines subjected to the same analysis permit some discrimination of the variation of atmospheric properties along the LOS.
 iv) The lines are only separated in wavelength by 1 Å, thus considerably reducing the spectral coverage of the detector relative to other line pairs.
  v) The lines fall in the red where CCD detectors typically have their highest quantum efficiency.
 vi) These lines have seen extensive use as magnetic-field diagnostics from ground-based instruments, so analysis techniques were in place and well-understood before the launch of *Hinode*.

The SP instrument was realized through collaboration of the principal contractor to NASA for the FPP (Lockheed Martin Solar and Astrophysics Laboratory) and the High Altitude Observatory of the National Center for Atmospheric Research, with significant interaction at all phases of design and construction by scientists at the National Astronomical Observatory of Japan.

Table 1 Spectro-polarimeter requirements and as-built performance.

Science requirement	Value	As-built	Science driver
Spectral resolution	≤ 35 mÅ	25 mÅ	Line widths in umbrae
Spectral sample	≤ 25 mÅ	21.55 mÅ	Resolve Stokes Profiles
Spectral coverage	≥ 2 Å @ 6302 Å	2.39 Å (normal) 4.77 Å (max)	Cover both 6301.5, 6302.5 Å plus high velocity events
Spatial coverage	$\geq 160''$	$162''$	Cover a typical active region
Polarization precision	$\leq 10^{-4}$	10^{-4} (average of 45 s, $0.5''$ sample)	Weak internetwork fields
Polarization S/N, contin.	$\geq 10^3$	910 in 4.8 s	Active region fields
Undispersed light scatter	$\leq 10^{-2}$	10^{-2} @ $\leq 10''$	Umbra/pore measurements
Spatial sample	$\leq 0.16''$	$0.1585''$ along slit $0.1476''$ slit step	Critical sampling of SOT resolution @ 6302 Å
Sampling cadence	≥ 10 Hz	10 Hz	Crosstalk arising from solar proper motions

2. Overall Design Concept

Table 1 presents the requirements for the SP as derived from the science requirements of the mission. These requirements led to the compact, lightweight, off-axis, reflecting Littrow spectrograph design shown in Figures 1, 2, and 3. In spite of its compact design, the SP meets the requirements set forth in Table 1 for precision solar spectro-polarimetry. This is achieved through the use of diffraction from the spectrograph slit to fill the grating, and through the use of a custom CCD detector optimized for dual-beam polarimetry.

3. Elements of the SP

3.1. The Polarization Modulator

The heart of the polarimetric systems for the FPP is the rotating retarder Polarization Modulator. It is located on the optical axis of the telescope between the Collimating Lens Unit of the Optical Telescope Assembly (OTA: Suematsu *et al.*, 2008, shown in red in Figure 1) and the Tip–Tilt Mirror. This placement of the modulator minimizes instrumental crosstalk among the Stokes parameters owing to the symmetry of the optical system and the low angles of reflection within the SOT. The modulator is a continuously rotating, multi-order bi-crystalline retarder with design retardations of $(5 + 0.35)$ waves at 6300 Å and $(7 - 0.35)$ waves at 5170 Å. This particular design (Guimond and Elmore, 2004) has several advantages. The two crystalline sapphire and quartz elements are radiation-tolerant and therefore are not expected to darken over an extended lifetime of the *Hinode* mission. This design has very low variation of retardance with both temperature and field-of-view. The quartz and sapphire optical elements are thin enough (1.597 and 1.371 mm, respectively) that any fringes present in monochromatic light will have a wavelength spacing much larger than the characteristic width of the solar spectrum lines, yet they are thick enough that they withstood dynamic testing and launch. Fringing from each of these vacuum-spaced elements is minimized by broadband anti-reflective coatings on the four surfaces. The selected retardance provides nearly equal modulation of Stokes polarization states Q, U, and V both at the SP
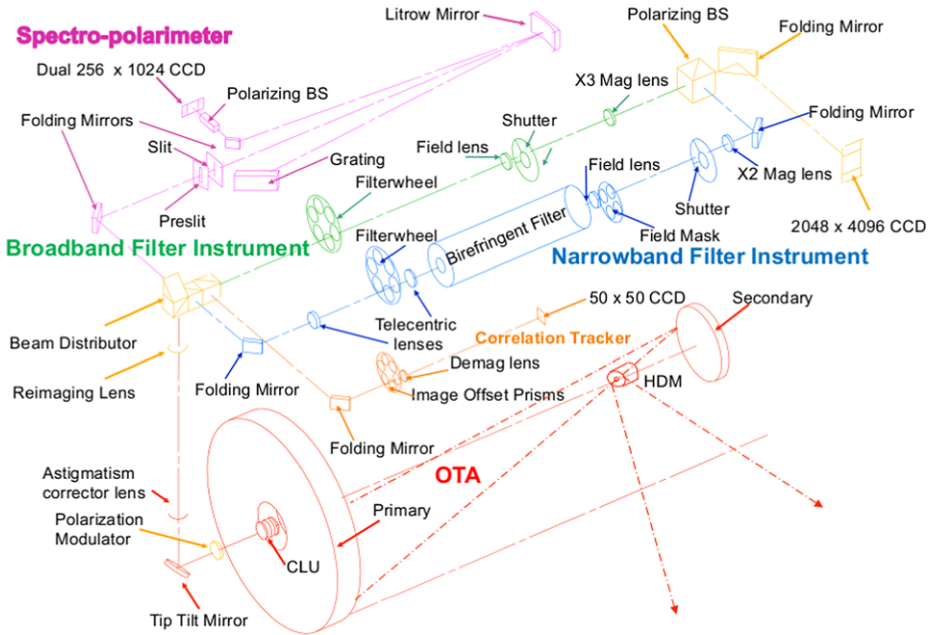
Optical layout of SOT

Figure 1 This optical schematic of the FPP shows the SP in magenta. The collimated, rotationally symmetric beam from the Optical Telescope Assembly (OTA: red) passes first through the Polarization Modulator, then is reflected toward the FPP by the Tip–Tilt Mirror. The Reimaging Lens forms a focus of the solar image on the SP slit, and the Beam Distributor sends roughly 43.5 % of the light at 6302 Å toward the spectrograph. The first Folding Mirror in the SP rotates about a vertical axis to scan the solar image across the slit. The Pre-slit, and the order isolation filter immediately behind it, prevent most of the unused energy from reaching the slit. The Littrow-configuration spectrograph is such that the Littrow Mirror serves as both a collimator and re-imager within the spectrograph. Although this schematic diagram is not to scale, the diameter of the primary mirror is 50 cm.

wavelength (6302 Å) and at the additional wavelength 5173 Å where the narrow-band filter (NFI) instrument also makes polarization measurements.

3.2. The Slit Scanning Mechanism

After the polarization modulator, the 45-degree reflections that divert the beam from along one of the spacecraft (x, y, z) axes to along another will not introduce crosstalk among the Stokes polarization parameters (Q, U, and V), provided that the final polarization analysis is also performed along these axes. In the case of the SP, this analysis is performed by the calcite polarizing beam splitter near the detector. The reflections of the Tip–Tilt mirror, the beam-distribution prism, and the slit-scan mirror are so oriented as to introduce minimal crosstalk. Furthermore, the slit-scan mirror is coated with a high-reflectivity protected silver coating, thereby also minimizing the polarization from this oblique reflection.

The FPP reimaging lens forms an image of the Sun at the spectrograph slit. The slit-scan mechanism can displace the solar image on the slit by up to $\pm 239''$ (on the Sun) in increments that average $0.148''$. To accomplish this small angular motion, a stepper motor drives a ball screw, which in turn drives motion-reducing levers mounted on flex pivots.
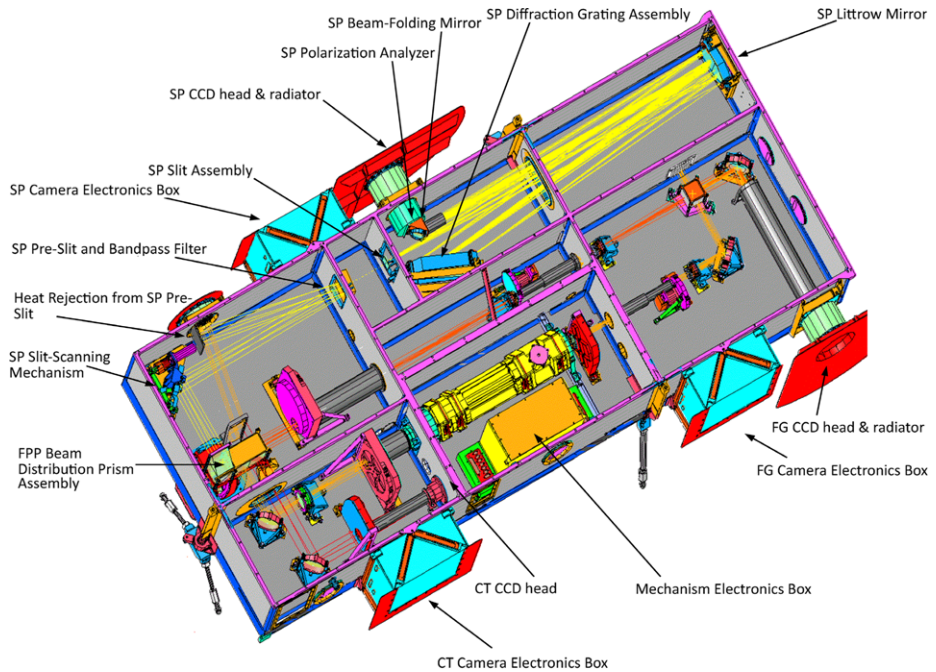
Figure 2 An isometric view of the design of the FPP is presented, showing ray-tracing beams through the optical elements. Elements of the SP are identified. See also Figures 1 and 3. The exterior length and width of the FPP structure box are 1625 mm and 649 mm, respectively.

The flex pivots minimize backlash. The image scanning does not occur at a pupil, so that the scan motion displaces the pupil image on the spectrograph grating. However, the range of the scan motion is small enough that the pupil displacement may be ignored, especially since the grating is significantly over-filled (see Section 3.4).

3.3. The Pre-Slit and Bandpass Filter

A reflective pre-slit assembly precedes the entrance slit of the spectrograph to reflect most of the broadband light and heat to a heat dump. A bandpass filter (FWHM = 10.0 Å, transmission = 0.934 at 6302 Å) is located at the pre-slit. This filter isolates the desired spectral order around 6302 Å to minimize stray undispersed light within the spectrograph.

3.4. An Off-Axis Reflecting Littrow Spectrograph

Weight and size constraints for space instrumentation dictate that the spectrograph be as compact as practical while still serving the scientific needs. A standard refracting Littrow spectrograph is appealing in that a single lens is employed for both collimation and reimaging of the beam. The *Hinode*/SP, as shown in Figure 3, uses a variant of the Littrow configuration where the lens is replaced by an off-axis paraboloid coated with protected silver. This makes the design more compact in the long dimension (925 mm focal length). It has the added advantages that it avoids stray-light reflections from the lens surfaces, and that focal properties are the same in either air or vacuum. The spectrograph slit is a 12 μm gap in an evaporated chromium layer on the flat surface of the plano-convex field lens (fused
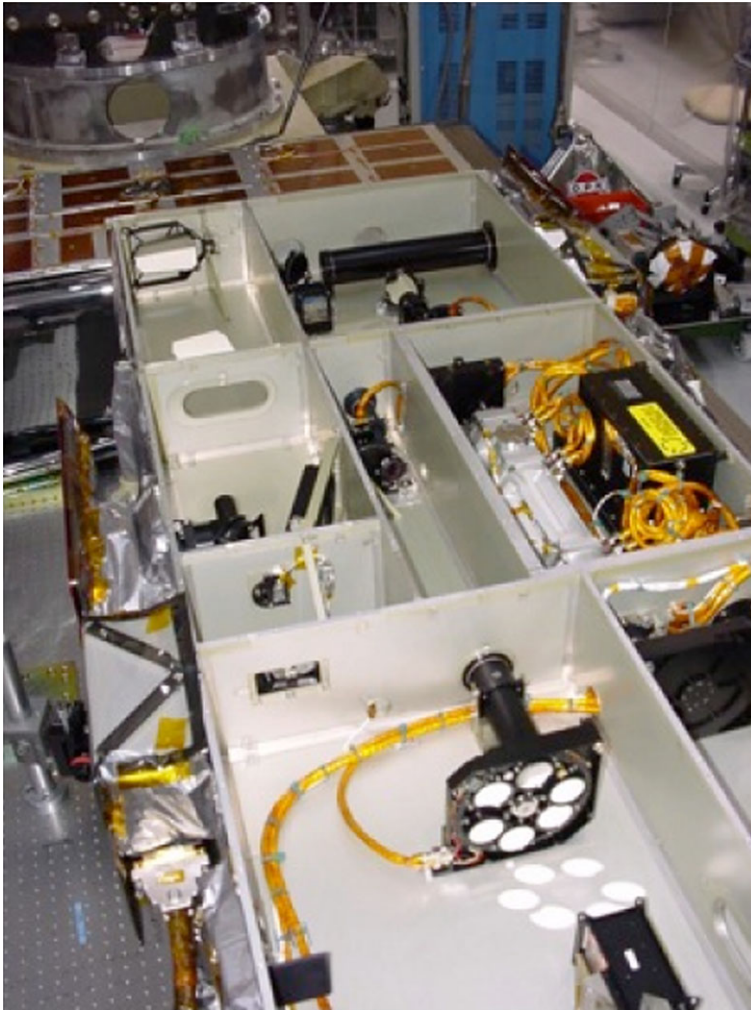
Figure 3 This view of the FPP with cover removed during testing and calibration, looking toward the SP Littrow mirror, shows the layout of the SP at the left inside of the box. At lower right is the beam-dividing prism. Not shown is the slit-scanning mechanism that is just below the bottom of this photograph. See Figures 1 and 2 to identify the elements of the SP in this photograph. The exterior width of the FPP structure box is 649 mm.

silica). The field lens immediately behind the slit images the pupil on the grating. Diffraction from the narrow slit fills the grating; without diffraction the f/31 beam incident on the slit would demand a much longer spectrograph in order to illuminate the grating and thus achieve the required spectral resolution. In this design only about 15 % of the light diffracted from the slit spills off the sides of the collimator and grating. The 79 line mm^{-1} echelle grating (aluminum coating) causes very little polarization at 6302 Å because it transmits *s*- and *p*-polarizations with nearly equal efficiency. A pick-off mirror directs the dispersed light returning from the grating toward the detector. This mirror surface is a dielectric coating optimized for high reflectivity at 6302 Å. It also assists in rejection of stray light at other wavelengths.

## 3.5. The Modified Savart Plate Polarization Analyzer

At the 10 Hz frame rate of the SP CCD camera, the evolution of the highly resolved solar scene can produce intensity variations at the few parts in 10^4 level during times comparable to the modulation cycle. Such variations, along with residual image motion of instrumental origin, may cause spurious polarization signals [$I \rightarrow Q, U$, and V crosstalk] if one analyzes the modulated beam with a single linear polarizer. This problem is largely overcome if one simultaneously analyzes both *s*- and *p*-polarizations, and combines the results appropriately in a "dual-beam" polarimeter (Lites, 1987; Judge *et al.*, 2004; Sankarasubramanian *et al.*, 2006; Gosain, 2007; Casini, de Wijn, and Judge, 2012). The advantages of dual-beam polarimetry in the presence of rapid seeing fluctuations have been demonstrated by several ground-based polarimeters including the ASP, and by the IMaX balloon-borne instrument (Martínez Pillet *et al.*, 2011). The SP implements this dual-beam approach via a modified Savart-plate polarizing beam splitter (Figure 4). The first element of the beam-splitter assembly is a weak cylindrical lens that partially compensates astigmatism introduced by the following calcite elements. The astigmatism of the modified Savart plate also is partially compensated by the off-axis nature of the spectrograph. The spectral mask that follows the cylindrical lens permits 4.6 Å of un-vignetted spectrum to proceed toward the detector. The two calcite elements, separated by a half-wave retarder, spatially separate the two orthogonal linear polarizations in the direction parallel to the spectral dispersion and, because of the mask, the restricted spectral range prevents the separate polarization images from overlapping at the detector. Each of the two crystals in the modified Savart plate is 27.0281 mm long. The calcite blocks and the wave plate are air-spaced, and each surface has anti-reflection "V" coats optimized for 6300 Å. The two sides of the CCD detector, onto which these two beams are imaged, henceforth are designated CCDSIDE0 and CCDSIDE1.

3.6. The CCD Camera

The SP CCD camera detectors and electronics were designed and fabricated specifically for this instrument by Marconi Applied Technologies of the UK (now e2v Technologies). The detector (Figure 5), with its two separate charge-collection and charge-storage areas, allows the camera to be read continuously at 10 Hz while shifting and reading a minimum number of pixels. This feature assists in minimizing the mean and peak power consumption of the cameras. The pixels are square with a linear dimension of 12 μm to match the width of the spectrograph slit. The spacing of the two active areas of the CCD in the spectral dimension derives from the optical design of the dual-beam spectrograph system. Frame transfer proceeds simultaneously in the same spectral direction for both polarization images in order that equivalent spectral pixels on the two sides of the CCD experience nearly the same rotational phases of the modulator. Shifting of the charge from the storage areas and A/D conversion occur sequentially for the two CCDSIDEs to reduce peak power consumption.

The camera readout electronics allow for summing one, two, or four pixels in either the serial or parallel direction during readout, but the flight software allows only for summing one or two pixels in the serial direction. The signals are digitized to a 12-bit precision. Digitization of selected sub-areas is permitted. From dark images taken on orbit, a read noise at the operational 10 Hz rate of 133 e$^-$ is achieved. The typical scale factor for SP data numbers (DN) using the default camera settings adopted since 2009 is about 76 e$^-$ per data number. The full-well capacity of the CCD is about 140 000 e$^-$, and typical quiet-Sun disk-center continuum levels at the start of the mission (see Figure 11) collected about 46 000 e$^-$ each 0.1-second exposure. Thus, the SP exposures always sit safely under the full-well limit.

Figure 4 The SP Polarizing Beamsplitter Assembly is shown in schematic view from a ray-tracing analysis. This system is known as a modified Savart plate. Two rays from differing spectral wavelengths (redward and blueward of the 6302 Å lines) are illustrated by lines of the corresponding colors. The *s* and *p* linear polarization states are separated spatially in the horizontal plane by the birefringent action of the calcite retarders and the half-wave plate. The spectral mask isolates a small range of the spectrum so that the *s*- and *p*-polarization images do not overlap at the focal plane. A weak cylindrical lens in front of the assembly corrects for the small amount of astigmatism from the calcite polarizing elements. Each of the two calcite blocks is 27.0281 mm long.

CCD

Calcite

Half Wave Retarder

Calcite

Spectral Mask

Cylindrical Lens
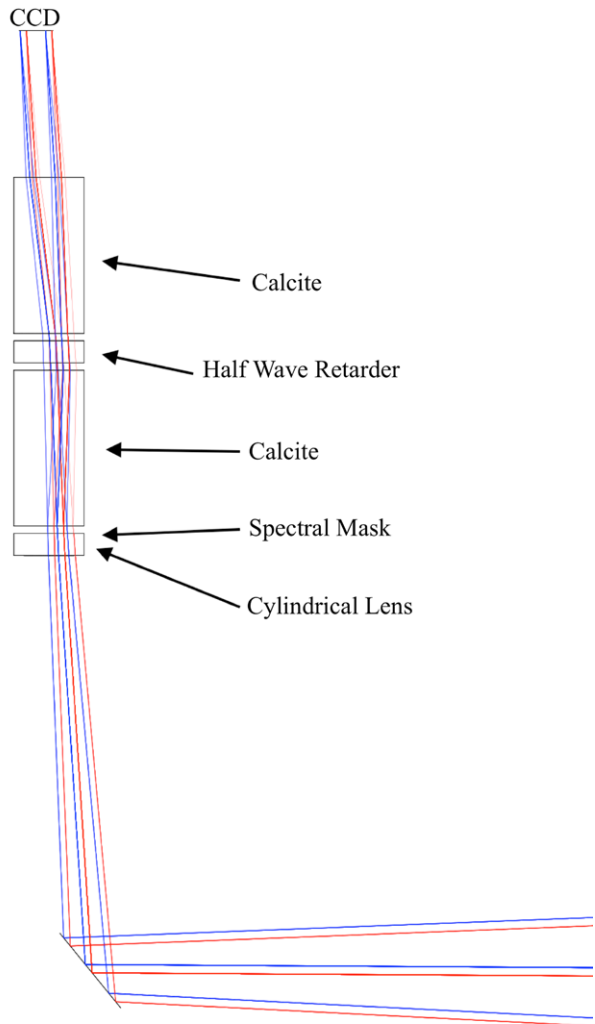
3.7. De-Modulation Electronics and On-Board Data Processing

The SP CCD camera records images and transmits them in digital form to the SP "smart memory" at a 10 Hz rate. The function of the smart memory is to "de-modulate" the polarization states that are temporally encoded, and to accumulate the polarization signals over several modulation cycles until the target S/N ratio is achieved. As illustrated by Lites (1987), the basic modulation cycle of the rotating retarder is half of one rotation, during which time eight images are transmitted from the CCD to the smart memory. The smart memory then adds or subtracts each image into four separate memory buffers, each buffer corresponding to one of the measured I, Q, U, and V Stokes parameters. The sign applied to the added value depends upon the buffer being addressed and upon the rotational phase of the modulator. The demodulation scheme is shown graphically and in table form for the eight-exposure scheme shown in Figure 22 of Ichimoto *et al.* (2008). This same demodula-
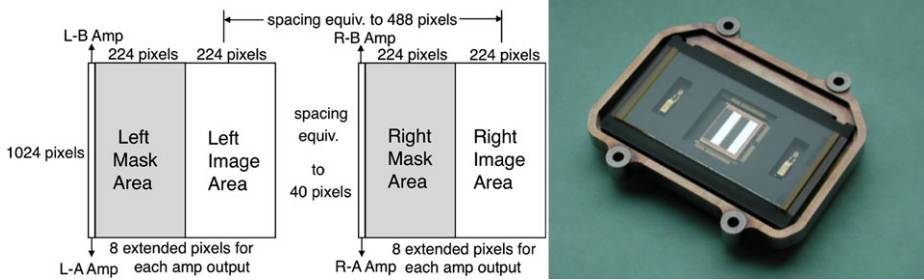
Figure 5 Right: the custom CCD chip for the SP in its housing is shown. Visible on the chip are the alternating mask (dark) and light-sensitive (white) areas. Left: a schematic of the layout of the chip is presented, showing the dimensions and separations of the light-sensitive and mask areas, and the locations of the four amplifiers. Two amplifiers are available for each image to provide redundancy. The long dimension of the active area is 12.288 mm.

tion scheme was used for the ASP (Elmore *et al.*, 1992). The size of the smart memory for the SP is eight Mbytes to allow for double-buffering of the data.

At the end of the accumulation cycle, typically three full rotations of the modulator or six modulation cycles, the raw accumulated-demodulated Stokes spectral images attain a polarization precision of about 10^{-3} (see Table 1). Each word in the smart memory is a two-byte integer, unsigned for Stokes I and signed for Stokes Q, U, and V. With the 12-bit digitization of each exposure and the actual intensity levels, digital overflow in the Stokes-I continuum occurs when the SP is programmed to carry out significantly longer accumulations than the typical 4.8 second "Normal Map" (see Section 6). This overflow is even more serious for data that are binned spatially (*i.e.* in the "Fast Map" observing mode). The smart memory therefore has the capability to bit-shift any of the buffers in order to avoid this digital overflow of the two-byte integers. Furthermore, the smart memory is able to "window" the data in the spatial direction (along the slit). The observer has a choice between 16 separate window sizes. Windowing permits the data volume to be reduced at its source for science programs that do not require the full 160″ spatial coverage along the slit.

Outside of the FPP itself, the Mission Data Processor (MDP) first does bit compression from 16 to 12 bits using look-up tables. This bit compression is based on square-root scaling, which preserves the data-digitization intervals relative to the noise. For normal operation the data are also subjected to lossy JPEG compression by the MDP to further reduce the data volume prior to downlink. Tests with ASP data early in the planning stages of the mission (see Figure 6) indicated that errors arising from JPEG compression of the Stokes spectra are significantly smaller than even the formal errors of the inversion (which in turn are typically smaller than systematic errors due to inadequacy of the Milne–Eddington model atmosphere). These tests showed that at the random noise levels of typical ASP data (a factor of two smaller than that from typical SP data), application of unrecoverable JPEG compression on-orbit does not compromise the inference of the magnetic-field vector; *i.e.* compression factors of about 10:1 do not seriously compromise the extraction of vector magnetic-field parameters. The on-orbit performance verifies this finding, and compression ratios of about 5:1 are typical for normal operations with real solar data from the SP.
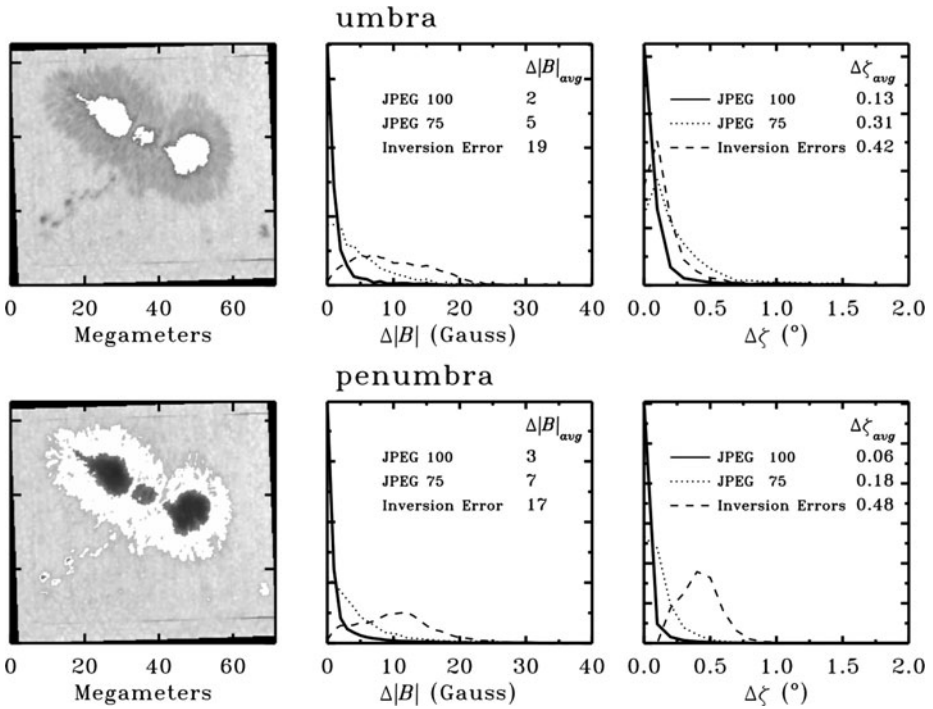
Figure 6 This figure presents the accuracy of inference of the magnetic-field strength when Stokes profile data are subjected to JPEG compression. The data used in these tests are from the ASP. The top (bottom) row of panels show distributions of error in the magnetic-field strength [$\Delta|B|$] and total angular departure of the field orientation [$\Delta\zeta$] as inferred by a Milne–Eddington inversion of the umbral (penumbral) data. The images on the left show continuum intensity, with the areas participating in the error distributions filled in solid white. The middle and right panels show the distributions of differences of inversion results with and without JPEG compression for field strength and orientation, respectively. Curves indicating the distributions of errors are shown for JPEG compression indices 100 (minimal compression) and 75 (moderate compression) are indicated by solid and dotted lines, respectively, and the curves in dashed lines show the formal inversion errors from the uncompressed data. The average rms departures from the inversions without compression are indicated on each panel, along with the average of the formal errors.

4. As-Built Performance of the SP

4.1. Spectral Resolution and Undispersed Stray Light

Prior to launch, the SP spectral-response profile was measured using a tunable laser, tuned to the vicinity of the 6302 Å Fe I lines. Due to wavelength drift of the tunable laser, short exposures were necessary to achieve reliable measures of the profile. Further, a rapidly rotating diffuser placed in front of the laser minimized the laser speckle pattern, and allowed more uniform illumination of the slit.

The curvature of the spectral lines along the slit may be used to obtain a spectral-response profile that is finely sampled in wavelength. In the spectral image of the laser emission, each pixel row (in the spectral direction) may be shifted to center the peak of the laser profile at a specified pixel. Further, the amplitude of the spectral emission for each row may be normalized. Because of the spectral curvature, superposition of the shifted and normalized laser profiles results in a spectral-response function that is finely sampled in wavelength. The

Figure 7 The dots show the measured laser profile for each CCSIDE of the SP, and the dashed lines are Gaussian fits with full width at half-maximum (FWHM) as indicated. Curvature of the spectrum along the slit allows one to obtain a spectral profile finely sampled in wavelength even though the actual spectral sampling is 21.549 mÅ.
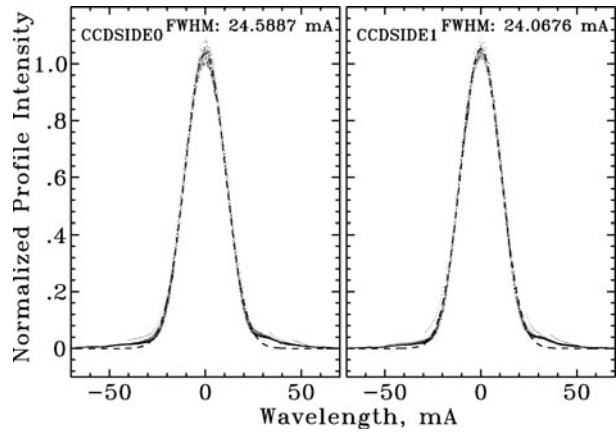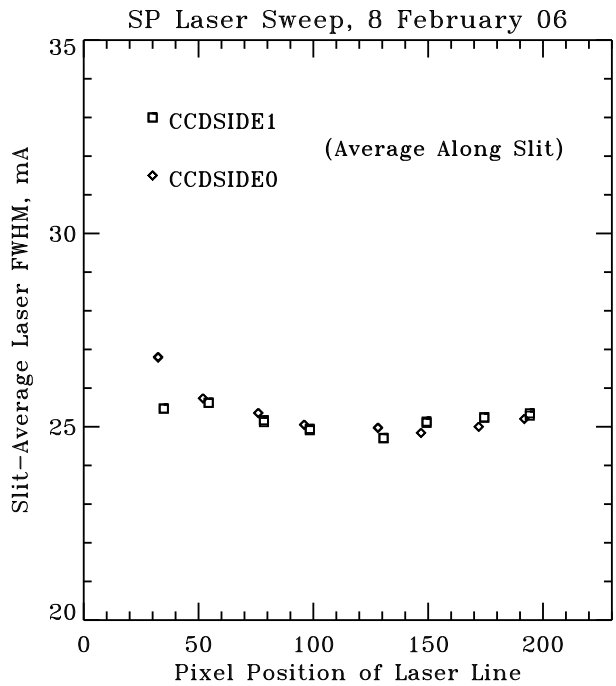
Figure 8 The variations of the measured laser profile widths, averaged over the length of the slit, are shown as a function of spectral pixel position for each CCDSIDE of the SP camera. The Fe I spectral lines at 6302 Å fall near the center of this pixel range.

profiles resulting from this analysis are shown in Figure 7 (dots). Gaussian fits to profiles are shown by the dashed lines, and the FWHM for each beam is indicated. These profiles, sampled near the center of the spectral range of the CCD, have FWHM ≈ 25 mA. Note the slight asymmetry in the red wing (expected from the off-axis spectrograph optical design) and somewhat elevated inner wings of the profiles relative to the Gaussian fits. These detailed measurements of the spectral response may be used in the analysis when fitting observed Stokes profiles.

Figure 8 presents the variation of the measured laser profile widths as a function of its position (in pixels) within the spectral field-of-view of both CCDSIDEs. There are small
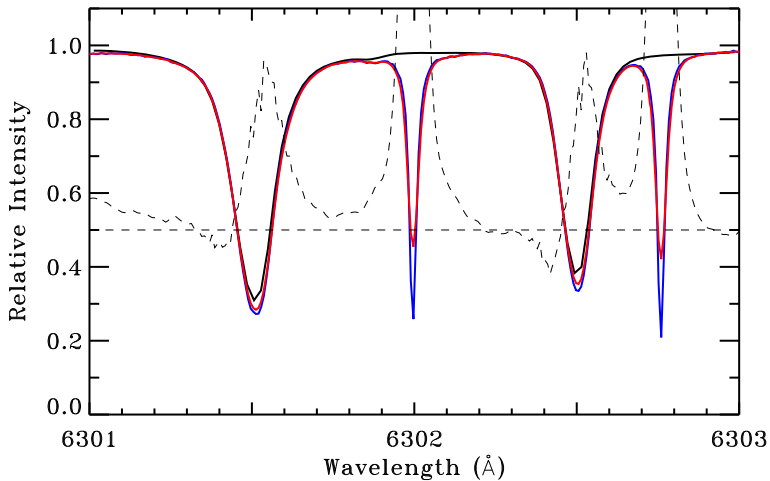
Figure 9 The observed quiet-Sun disk-center *Hinode*/SP spectral profile is plotted in black, along with the corresponding NSO FTS spectral profile (blue). The red curve shows the result of convolution of the FTS profile with the measured SP instrument spectral-response function (see Figure 7). The dashed curve is the observed SP spectral profile minus the convolved FTS profile, multiplied by a factor of 10 and offset with an additive factor of 0.5. The straight, dashed horizontal line at 0.5 shows the zero level for the latter difference of profiles.

variations within the spectral field that have minimal influence on the measured profiles. The variation of the profile widths along the slit are similarly insignificant.

Even though the spectral resolution profile may not be measured on-orbit, one may check for gross problems by comparing the observed profiles with those measured precisely from the ground. Figure 9 presents the FTS atlas (Wallace, Hinkle, and Livingston, 1998) of the region around the 6300 Å spectrum lines, along with an average disk-center Stokes-*I* spectral profile from the *Hinode*/SP. Figure 9 also shows the FTS profile convolved with the measured SP instrument spectral-response function (see Figure 7). The observed profiles from the SP (black) are about 3 % of the continuum intensity brighter at line center than the convolved FTS atlas profiles as indicated by the dashed curve in Figure 9, which shows the difference between the observed SP Stokes-*I* profile and the convolved FTS profile, multiplied by a factor of ten. A possible contributor to the brighter SP line-core intensity could be undispersed stray light in the spectrograph, but such stray light should be minimal owing to the narrow order-isolation filter in front of the spectrograph slit. The comparison of FTS and observed spectral profiles presented in Figure 9 establishes an upper limit on undispersed stray light at about 3–4 % of the continuum intensity. Comparing the FTS and SP profiles, one sees slight differences in the shapes of the line cores. These differences could arise from the limited sample of the profiles in the SP data, which are selected from the quiet Sun excluding regions of high polarization signal.

4.2. Slit Scan Linearity

Two-dimensional maps of the magnetic-field vector are built up from SP data via motion of the slit-scan mirror. Prior to integration into the FPP, the linearity of the slit scan mechanism was calibrated optically in the laboratory using a theodolite, and later verified by comparison of SP maps of an optical target with simultaneous FG images. The slit scan has a periodic

Figure 10 The departure of the slit-scan angular deflection from a linear dependence is shown for laboratory theodolite measurements over the full range of the slit scanner. The ordinate is presented in arcseconds in the laboratory, which is 13.3 times larger than the corresponding deflection of the solar image. The periodic departure from linearity is due to an error in the ball screw mechanism.
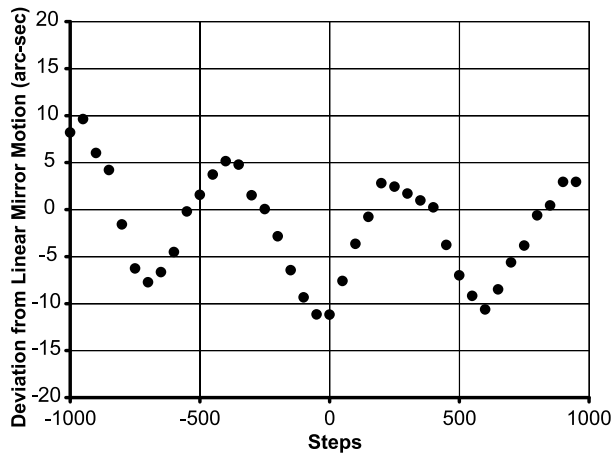
error of amplitude a little more than one arcsecond (on the Sun) peak-to-peak due to an error in the ball-screw mechanism. The period of this error is about 650 steps of the scanner (Figure 10), corresponding to about $100''$ on the Sun.

In a detailed analysis of coalignment between the SP and the Filtergraph instruments, Centeno *et al.* (2009) derived the on-orbit behavior of the periodic error in the slit scan to high accuracy. Reported in that article are functions that not only characterize the periodic error, but other spatial effects as well.

4.3. Throughput and Polarization Signal-to-Noise (S/N)

On-orbit one is able to quantify the S/N by measuring the fluctuation of the signal in the continuum of the demodulated Q, U, and V polarizations. The expected polarization signals of the intrinsic solar spectral continuum at disk center are very much smaller than the $\approx 10^{-3}$ noise level of a typical SP measurement. Polarization in the continuum arising from instrumental effects is removed prior to these estimations of rms fluctuation by the standard SP calibration procedures (Lites and Ichimoto, 2012).

Figure 11 presents the flux history of the SP along with the corresponding measurements of noise in the polarization continua. Most of these data are extracted from the *Hinode* Observing Program (HOP) 79 (listed as HOP 46 early in the mission) Solar Irradiance program. This program is executed approximately every month, and produces SP maps covering from the N to S Poles along the central meridian. The data are taken in an identical manner starting in October 2008. Before that time, Figure 11 presents the same analysis of measurements taken in the quiet Sun at disk center. Few appropriate maps were obtained during the middle of 2008.

The observations shown with black diamonds in Figure 11 represent the mean signal level of the Stokes-*I* continuum, per pixel per second, in SP data numbers (DN – see scale at left of graph). The SP throughput is decreasing in a linear fashion, as shown by the linear fit of these data, at a rate of -251 DN yr^{-1}. It has decreased about 17 % in the five years after launch shown in this analysis.

Beginning in 2008, the recommended settings for the SP camera digital–analog converter offsets (DAC) were changed. The offset used as the default during the early part of the mission (DAC ID $= 7$) added a large value to the observations that occasionally resulted in digital wrap-around of the 16-bit integer intensities for long SP observations. To minimize
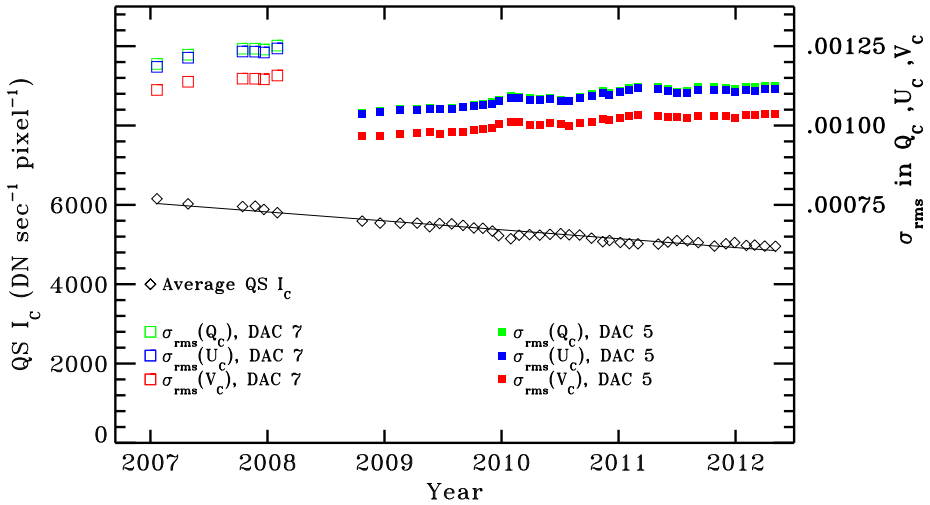
Figure 11 The average level of the quiet-Sun continuum at disk center as seen by the SP is shown by the black diamonds. The black, straight line represents a linear fit through these points. The vertical axis at left shows the signal levels in DN for the SP per pixel per second. Colored squares represent the rms fluctuation in the polarization continua relative to the continuum Stokes I: Q (green), U (blue), and V (red) for the typical SP observation of 4.8-second exposure (see text). Open squares, early in the mission, flag measurements with analog–digital converter offset parameter 7, whereas later in the mission the small filled squares represent observations at a different offset (offset parameter 5). The vertical axis labels at right indicate the level of fluctuation in the polarization continua.

the occurrence of this wrap-around, the default offset was reset to the offset assigned to DAC ID = 5, resulting in much lower offsets.

The rms fluctuation of the polarization continua in level1 data is shown as the colored open squares for DAC ID = 7, and as the filled smaller squares for DAC ID = 5. Evidently the newer offset reduces the noise somewhat especially considering that the data prior to 2008 were obtained with both CCDSIDEs, whereas the more recent data recorded only one CCDSIDE, but are summed two pixels along the length of the slit. The single-sided data selects CCDSIDE0 – the beam that has the higher intensity throughput of the two beams. To arrive at these estimates, only the spectral regions away from the lines were considered, and pixels having significant Stokes-V polarization were also excluded because the latter produce polarization throughout the entire 2.39 Å spectral range of a typical SP observation. The slight increase in noise over the years reflects the decreasing throughput of the SP. Note that the noise levels in Q are nearly identical to those in U, but that the noise is somewhat smaller in V, probably owing to the approximately 8 % higher modulation efficiency in Stokes V relative to Q and U (Ichimoto *et al.*, 2008). As of mid-August 2011, the S/N stood at 890 for Stokes Q and U and 950 for Stokes V.

Figure 11 presents the history of the rms fluctuation in polarization applicable for two-sided level1 data without summing along the slit, or single-sided data that are summed two pixels along the slit, for the standard SP exposure time of 4.8 seconds (three full rotations of the polarization modulator). These data may be used to estimate noise levels in polarization for observations having different exposure times, different summing along the slit, or different binning in the slit scan direction (*e.g.* Fast Maps), when they are scaled according to the square-root of the total number of photons summed in the observation.
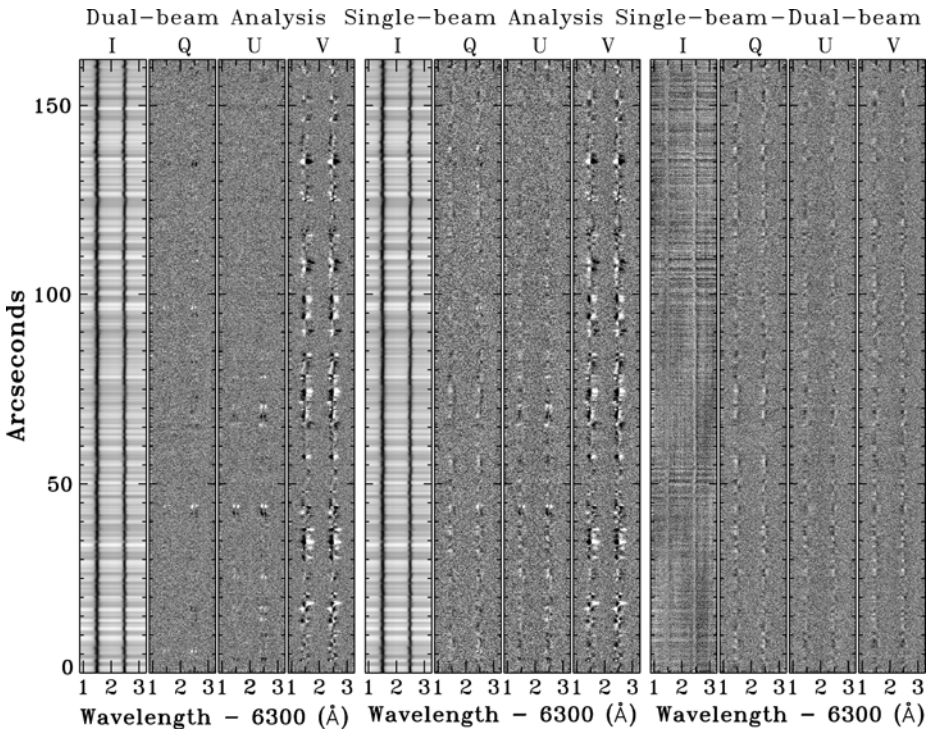
Dual−beam Analysis Single−beam Analysis Single−beam−Dual−beam

I Q U V I Q U V I Q U V

Figure 12 The relative performance of the *Hinode*/SP operating in single- and dual-beam modes is illustrated by analysis of intrinsically dual-beam data from 10 March 2007. The left panel displays the level1 Stokes spectra where both beams are included in the analysis; the middle panel shows the result of processing only a single beam. The right panel presents the difference between the two analyses. Stokes-I images in the left two panels are scaled by their full range, whereas the Q, U, and V images are scaled to saturate at ± 0.003 I_C, as are the Q, U, and V difference images in the right panel. The Stokes-I difference image is scaled ± 0.01 I_C.

The severe reduction of the *Hinode* telemetry rate following failure of the onboard X-band transmitter in December 2007 (Shimizu, 2009) dictated that new strategies in *Hinode* observing be implemented. In order to conserve telemetry, most observations after early 2008 have been carried out in single-beam mode, where data from only one of the CCD-SIDEs are transmitted to the ground. This restriction on the data results in an increase in the noise level, but also some increase in $I \rightarrow Q, U$, and V crosstalk arising from residual image motion and plasma motions on the Sun is experienced when using a single beam only. In practice, however, the *Hinode* correlation tracker has excellent performance (Shimizu *et al.*, 2008) so that this additional source of crosstalk may be ignored except for observations of quiet regions requiring the smallest noise levels.

The performance of the SP operating in single-beam mode relative to that when operating in dual-beam mode is illustrated in Figures 12 and 13. Figure 12 presents the results of processing intrinsically dual-beam quiet-Sun data, first taking into account both beams (left panel of Figure 12), then considering only one of the two beams (middle panel of Figure 12). It should be noted that a significant amount of $I \rightarrow Q, U$, and V crosstalk is eliminated by the standard SP calibration procedure even in the single-beam analysis. That process determines the wavelength-averaged level of continuum polarization in Q, U, and V, and
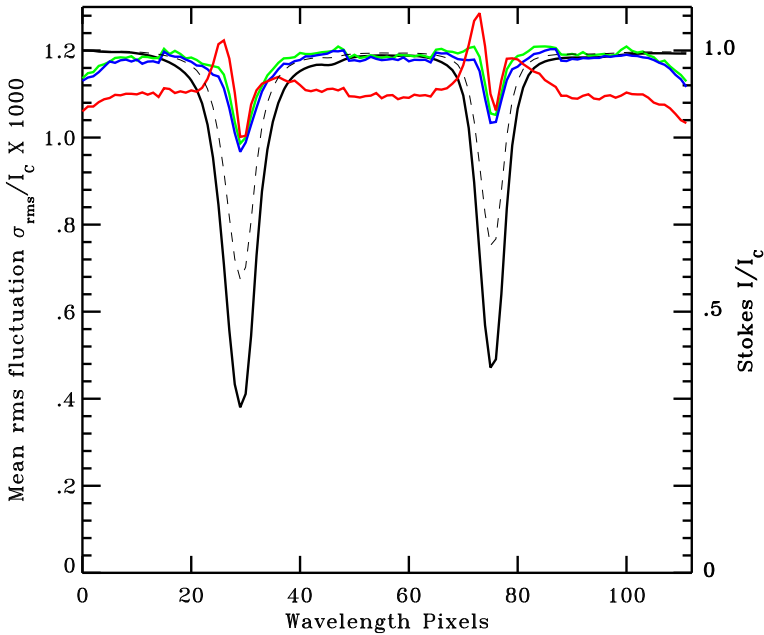
Figure 13 The wavelength variations of the rms fluctuation in the polarization Q, U, and V arising from residual image motion are shown as green, blue, and red lines, respectively. These variations were derived from the difference of single- and dual-beam analysis of the same data (see difference image in right panel of Figure 12). The black solid curve is the mean spectral profile normalized to its continuum (scale on right of plot). The dashed black line represents the square root of the intensity profile, indicating the expected relative level of the fluctuations in polarization arising from random noise (see text). Plotted curves represent the average over 100 steps of the SP map for which one frame is presented in Figure 12.

adjusts the spectra on a row-by-row basis to eliminate crosstalk from residual image motion. See Lites and Ichimoto (2012) for a description of that processing, and in particular see Figure 9 of that article where the row-by-row continuum crosstalk due to image motion is visible in the raw data of each beam. The middle panel of Figure 12 has higher noise at continuum wavelengths than the left panel as a result of detection of about half the number of photoelectrons. Closer examination shows that there are signals present in Q and U at the line centers in the single-beam panel that are absent in the dual-beam analysis. The difference image in the right panel shows that these spurious signals are present also in Stokes V. They arise from residual image motion (or from the intrinsic evolution of the solar scene) in which Doppler shifts at small scales cause the line profiles to fluctuate during the modulation cycle. Such Doppler-induced crosstalk is not corrected by the standard SP reduction procedure, which is based on polarization of the continuum only. Thus this source of spurious polarization remains as a feature of the SP data taken in single-beam mode.

To further quantify this degradation of the data quality in single-beam mode, Figure 13 shows the rms fluctuation of the difference between the single- and dual-beam analyses as a function of wavelength. First consider the black solid line in that figure (the normalized mean spectral profile), and the black dashed line (the square root of the normalized Stokes-I profile). The latter represents the rms noise relative to the noise in the continuum were the signal arising entirely from photoelectrons. In fact, there is a small amount of read noise amounting to about 0.6 % of the signal in the continuum and 2.1 % in the core of the deeper
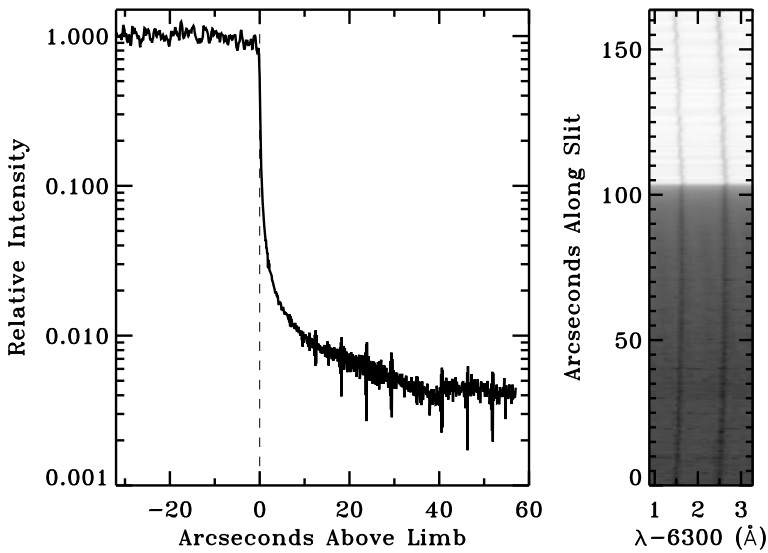
Figure 14 Right: a spectral image from the SP taken during solar eclipse is displayed using a logarithmic intensity scale. The display shows the solar absorption lines above the limb (*i.e.* downward below 105″ in the image) arising from scattering within the SOT/FPP optics. Left: the continuum intensity as a function of distance of each plotted slit position above the lunar limb is plotted. The intensity above the limb falls below 0.01 of the disk intensity at about 10″ above the limb.

of the spectral lines (see Section 3.6). For qualitative illustration here, these levels of read noise may be ignored. The colored line plots display the statistical fluctuation along the slit direction of the Q, U, and V single- minus dual-beam difference images as averaged over 100 separate observations of the quiet-Sun data set. If there were no additional crosstalk due to Doppler shifts and image motion, the colored plots would be expected to approximately follow the black dashed curve.

It is evident from the above analysis that the single-beam observations suffer a degradation of the polarization signals within the line cores of a few parts in 10^3. This will compromise observations of the very quiet Sun, but for maps of active regions the polarization signals are usually large enough that these small effects may be ignored.

4.4. Instrumental Scattered Light

The narrow-band filter in front of the spectrograph drastically reduces the light entering the spectrograph from undesired wavelengths. This, coupled with the minimal scattering properties of the off-axis Littrow spectrograph design (Section 3.4), keeps nearly all undispersed light from reaching the detector (see Section 4.1 for an estimate of the amount of undispersed stray light). Light scattered in the OTA and optics leading up to the spectrograph therefore will be spectrally dispersed before reaching the SP detector. This is demonstrated by Figure 14 showing a single spectral observation taken during a partial solar eclipse. These observations give us an excellent opportunity to quantify the scattering properties of the optics feeding the spectrograph.

The observations shown in Figure 14 were obtained on 11 July 2010 during the total solar eclipse seen from Earth. The *Hinode* spacecraft experienced three partial eclipses during three successive orbits on that day, the data considered here were taken during the third
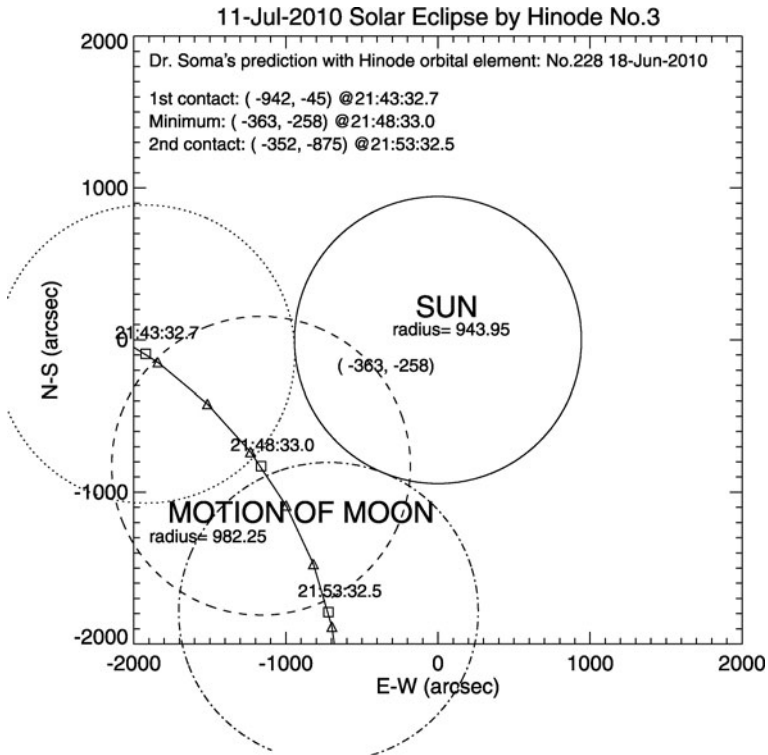
Figure 15 The path of the lunar disk against the solar disk is shown for the third such eclipse of the Sun as seen by *Hinode* on 11 July 2010. The lunar disk (dot–dashed) is shown for three times: first, contact, maximum obscuration (labeled "minimum"), and second contact. The SP slit, oriented in the solar North–South direction, was positioned near the point of furthest penetration of the lunar disk onto the solar disk, as labeled (−363, −258), corresponding to arcseconds West and North of solar disk center. At that time and point on the solar disk, the motion of the Moon along the SP slit reaches a standstill. Observations at that time are used to examine the scattered light in the SOT optical system. (Courtesy of M. Soma.)

eclipse. Figure 15 shows a prediction of the path of the Moon over the solar disk as seen by *Hinode* for that eclipse. The SP slit, oriented North–South on the Sun, was held steady at the spacecraft coordinates [−368, −271] (arcseconds West and North of disk center, respectively), close to the position of maximum obscuration of the solar disk as seen by *Hinode*. This position was selected because there the motion of the lunar limb in the N–S direction comes to a halt at the time of maximum partial eclipse.

The spacecraft orbital motion ensures that the apparent motion of the lunar disk across the Sun is very fast. In order to attain good statistics of the scattered-light intensity, the observations were planned for the full length of the slit (only one CCDSIDE) without binning along the slit. At the time of maximum eclipse when the motion of the lunar disk along the slit has halted, one may attain good resolution of the lunar limb as shown in Figure 14.

In order to determine the level of scattering, the dark level of the SP detector must be well known. The 11 July 2010 solar eclipse occurred during the height of the *Hinode* spacecraft eclipse season when the Sun is obscured by the Earth for a few minutes every orbit. Thus, SP measurements of the SOT viewing the Earth provide an excellent dark level (Lites and

Ichimoto, 2012). Such measurements were obtained between 21:35 and 21:40 UT, just prior to the observations shown in Figure 14 at 21:48 UT.

The image at right in Figure 14 shows the raw SP data corrected only for dark level and displayed on a logarithmic scale to reveal structure of the image above the limb. The observations are "normal mode" (see Section 6) having a 4.8-second exposure. The Fe I lines are seen in absorption all the way to the extreme bottom of the detector. There, the depths of the spectrum lines are comparable to those of the same exposure on the solar disk, indicating that the dark-level correction is adequate. A plot of the mean continuum level as a function of height above the solar limb (corrected for the tangent to the limb at mid-eclipse) is shown in the left panel of Figure 14. The curve falls very rapidly just above the limb, presumably owing to the diffraction pattern of the *Hinode*/SOT. The excellent optical quality of the SOT/SP combination was already evident in the solar-limb measurements reported by Lites *et al.* (2010), as was the scattered-light spectrum from the solar disk. The scattered light in this measurement falls below 10^{-2} at about $10''$ above the lunar limb.

This measurement will permit extraction of the contribution to the point-spread function for the SP arising from scattering. In turn, an accurate assessment of that function will permit more detailed analyses of magnetic-field structure below the angular resolution of the SP because the influence of scattering from its surroundings will be known.

5. SP Polarization Calibration

Polarization calibration of the SP is described by Ichimoto *et al.* (2008). Calibration procedures for flat-field and dark correction, residual polarization crosstalk correction, merging of the dual-beam images, correction for spectral curvature and skew, and compensation for thermal flexure of the instrument as determined on-orbit are described in the companion article (Lites and Ichimoto, 2012).

6. SP Observing Modes

The *Hinode*/SP is simple in design, and allows only a few observing modes. Nonetheless, the flexibility of slit scanning and binning allows the instrument to address diverse problems in solar physics. The four basic SP observing modes are summarized as follows.

Normal Mode: Typical integration times to reach continuum S/N = 1000 in Q, U, and V is 4.8 seconds, or three full rotations of the modulator. The slit scanner then steps after accumulating data for three rotations. This mode is most useful for maps of the vector magnetic field of active regions. A 1024 × 1024 [$151'' × 162''$] map requires about 90 minutes to execute.

Fast Map Mode: Frequently there is need to accomplish maps of the vector magnetic field more rapidly than the Normal Mode. The Fast Map mode bins two pixels along the slit at the camera, then sums each two successive integrations in Smart Memory, resulting in spatial samples $0.30'' × 0.32''$. In this mode the slit scanner is stepped one step after each rotation of the modulator (1.6 seconds), thus each measurement comprises the sum of two successive slit position measurements. A $151'' × 162''$ Fast Map requires about 30 minutes.

Dynamics Mode: For exploration of very rapid changes in the photosphere at small scales, allowance was made for the Dynamics Mode in which integration is carried out for only a single rotation of the modulator. These data are collected at reduced S/N. Data-rate constraints at the spacecraft demand that the spectral images be windowed to eliminate at least 2/3 of the full 1024-pixel slit length of the Normal Mode.

Deep Magnetogram Mode: This mode facilitates studies of weak internetwork. It permits the polarization signal to be integrated over many rotations of the modulator. For example, $S/N = 10^4$ in Q, U, and V may be attained in four minutes with two-pixel summing along the direction of the slit. In extremely long integrations of the Deep Magnetogram Mode, one anticipates that both Stokes-I and regions of large Stokes-V polarization signal may digitally "wrap around" beyond the 16-bit dynamic range of the smart memory. Allowance is made in the flight software to bit-shift any or all of the four Stokes parameters as they are accumulated in order to avoid digital wrap-around (see Section 3.7). In order to avoid wrap-around for very long exposures, it is recommended to keep the total exposure of a Normal Map to less than 12.8 seconds, and of a Fast Map to less than 6.4 seconds. To achieve longer integrations, successive measurements must be summed in data processing of the downlinked data.

References

Bellot Rubio, L.R.: 2006, In: Casini, R., Lites, B.W. (eds.) *Solar Polarization 4* **CS-358**, Astron. Soc. Pac., San Francisco, 107.

Casini, R., de Wijn, A.G., Judge, P.G.: 2012, *Astrophys. J.* **757**, 45. doi:10.1088/0004-637X/757/1/45.

Centeno, R., Lites, B., de Wijn, A.G., Elmore, D.: 2009, In: Lites, B., Cheung, M., Magara, T., Mariska, J., Reeves, K. (eds.) *The Second Hinode Science Meeting: Beyond Discovery – Toward Understanding* **CS-415**, Astron. Soc. Pac., San Francisco, 323.

Elmore, D.F., Lites, B.W., Tomczyk, S., Skumanich, A.P., Dunn, R.B., Schuenke, J.A., Streander, K.V., Leach, T.W., Chambellan, C.W., Hull, H.K.: 1992, In: Goldstein, D.H., Chipman, R.A. (eds.) *Polarization Analysis and Measurement*, *SPIE Conf. Ser.* **1746**, 22.

Gosain, S.: 2007, PhD thesis, Udaipur Solar Observatory, Mohanlal Sukhadia University. http://www.openthesis.org/documents/Polarimetric-Studies-Solar-Atmosphere-601238.html

Guimond, S., Elmore, D.F.: 2004, *OE Mag.* **4**(5), 26.

Ichimoto, K., Lites, B., Elmore, D., Suematsu, Y., Tsuneta, S., Katsukawa, Y., Shimizu, T., Shine, R., Tarbell, T., Title, A., Kiyohara, J., Shinoda, K., Card, G., Lecinski, A., Streander, K., Nakagiri, M., Miyashita, M., Noguchi, M., Hoffmann, C., Cruz, T.: 2008, *Solar Phys.* **249**, 233. ADS:2008SoPh..249..233I, doi:10.1007/s11207-008-9169-9.

Judge, P.G., Elmore, D.F., Lites, B.W., Keller, C.U., Rimmele, T.: 2004, *Appl. Opt.* **43**, 3817. doi:10.1364/AO.43.003817.

Kosugi, T., Matsuzaki, K., Sakao, T., Shimizu, T., Sone, Y., Tachikawa, S., Hashimoto, T., Minesugi, K., Ohnishi, A., Yamada, T., Tsuneta, S., Hara, H., Ichimoto, K., Suematsu, Y., Shimojo, M., Watanabe, T., Shimada, S., Davis, J.M., Hill, L.D., Owens, J.K., Title, A.M., Culhane, J.L., Harra, L.K., Doschek, G.A., Golub, L.: 2007, *Solar Phys.* **243**, 3. ADS:2007SoPh..243....3K, doi:10.1007/s11207-007-9014-6.

Lites, B.W.: 1987, *Appl. Opt.* **26**, 3838. doi:10.1364/AO.26.003838.

Lites, B.W., Casini, R., Manso Sainz, R., Jurčák, J., Ichimoto, K., Ishikawa, R., Okamoto, T.J., Tsuneta, S., Bellot Rubio, L.: 2010, *Astrophys. J.* **713**, 450. doi:10.1088/0004-637X/713/1/450.

Lites, B.W., Ichimoto, K.: 2012, *Solar Phys.* doi:10.1007/s11207-012-0205-4.

Martínez Pillet, V., Del Toro Iniesta, J.C., Álvarez-Herrero, A., Domingo, V., Bonet, J.A., González Fernández, L., López Jiménez, A., Pastor, C., Gasent Blesa, J.L., Mellado, P., Piqueras, J., Aparicio, B., Balaguer, M., Ballesteros, E., Belenguer, T., Bellot Rubio, L.R., Berkefeld, T., Collados, M., Deutsch, W., Feller, A., Girela, F., Grauf, B., Heredero, R.L., Herranz, M., Jerónimo, J.M., Laguna, H., Meller, R., Menéndez, M., Morales, R., Orozco Suárez, D., Ramos, G., Reina, M., Ramos, J.L., Rodríguez, P., Sánchez, A., Uribe-Patarroyo, N., Barthol, P., Gandorfer, A., Knoelker, M., Schmidt, W., Solanki, S.K., Vargas Domínguez, S.: 2011, *Solar Phys.* **268**, 57. ADS:2011SoPh..268...57M, doi:10.1007/s11207-010-9644-y.

Sankarasubramanian, K., Lites, B., Gullixson, C., Elmore, D., Hegwer, S., Streander, K., Rimmele, T., Fletcher, S., Gregory, S., Sigwarth, M.: 2006, In: Casini, R., Lites, B.W. (eds.) *Solar Polarization 4* **CS-358**, Astron. Soc. Pac., San Francisco, 201.

Shimizu, T.: 2009, In: Lites, B., Cheung, M., Magara, T., Mariska, J., Reeves, K. (eds.) *The Second Hinode Science Meeting: Beyond Discovery-Toward Understanding* **CS-415**, Astron. Soc. Pac., San Francisco, 1.

Shimizu, T., Nagata, S., Tsuneta, S., Tarbell, T., Edwards, C., Shine, R., Hoffmann, C., Thomas, E., Sour, S., Rehse, R., Ito, O., Kashiwagi, Y., Tabata, M., Kodeki, K., Nagase, M., Matsuzaki, K., Kobayashi, K., Ichimoto, K., Suematsu, Y.: 2008, *Solar Phys.* **249**, 221. ADS:2008SoPh..249..221S, doi:10.1007/s11207-007-9053-z.

Snik, F., de Wijn, A.G., Ichimoto, K., Fischer, C.E., Keller, C.U., Lites, B.W.: 2010, *Astron. Astrophys.* **519**, A18. doi:10.1051/0004-6361/201014500.

Suematsu, Y., Tsuneta, S., Ichimoto, K., Shimizu, T., Otsubo, M., Katsukawa, Y., Nakagiri, M., Noguchi, M., Tamura, T., Kato, Y., Hara, H., Kubo, M., Mikami, I., Saito, H., Matsushita, T., Kawaguchi, N., Nakaoji, T., Nagae, K., Shimada, S., Takeyama, N., Yamamuro, T.: 2008, *Solar Phys.* **249**, 197. ADS:2008SoPh..249..197S, doi:10.1007/s11207-008-9129-4.

Tsuneta, S., Ichimoto, K., Katsukawa, Y., Nagata, S., Otsubo, M., Shimizu, T., Suematsu, Y., Nakagiri, M., Noguchi, M., Tarbell, T., Title, A., Shine, R., Rosenberg, W., Hoffmann, C., Jurcevich, B., Kushner, G., Levay, M., Lites, B., Elmore, D., Matsushita, T., Kawaguchi, N., Saito, H., Mikami, I., Hill, L.D., Owens, J.K.: 2008, *Solar Phys.* **249**, 167. ADS:2008SoPh..249..167T, doi:10.1007/s11207-008-9174-z.

Wallace, L., Hinkle, K., Livingston, W.: 1998, *An atlas of the spectrum of the solar photosphere from 13,500 to 28,000 cm^{-1} (3570 to 7405 A)*, Nat. Solar Obs.